

# Influence of Noise on Scattering-Parameter Measurements

**Citation for published version (APA):**

Gu, D., Jargon, J., Ryan, M., & Hubrechs, A. (2020). Influence of Noise on Scattering-Parameter Measurements. *IEEE Transactions on Microwave Theory and Techniques*, 68(11), 4925-4939.  
<https://doi.org/10.1109/TMTT.2020.3014627>

**DOI:**

[10.1109/TMTT.2020.3014627](https://doi.org/10.1109/TMTT.2020.3014627)

**Document status and date:**

Published: 01/11/2020

**Document Version:**

Accepted manuscript including changes made at the peer-review stage

**Please check the document version of this publication:**

- A submitted manuscript is the version of the article upon submission and before peer-review. There can be important differences between the submitted version and the official published version of record. People interested in the research are advised to contact the author for the final version of the publication, or visit the DOI to the publisher's website.
- The final author version and the galley proof are versions of the publication after peer review.
- The final published version features the final layout of the paper including the volume, issue and page numbers.

[Link to publication](#)

**General rights**

Copyright and moral rights for the publications made accessible in the public portal are retained by the authors and/or other copyright owners and it is a condition of accessing publications that users recognise and abide by the legal requirements associated with these rights.

- Users may download and print one copy of any publication from the public portal for the purpose of private study or research.
- You may not further distribute the material or use it for any profit-making activity or commercial gain
- You may freely distribute the URL identifying the publication in the public portal.

If the publication is distributed under the terms of Article 25fa of the Dutch Copyright Act, indicated by the "Taverne" license above, please follow below link for the End User Agreement:

[www.tue.nl/taverne](http://www.tue.nl/taverne)

**Take down policy**

If you believe that this document breaches copyright please contact us at:

[openaccess@tue.nl](mailto:openaccess@tue.nl)

providing details and we will investigate your claim.

# Influence of Noise on Scattering-Parameter Measurements

Dazhen Gu, Jeffrey Jargon, Matthew Ryan and Anouk Hubrechsens

**Abstract**—We present a general model of noisy scattering-parameter (S-parameter) measurements performed by a vector network analyzer (VNA). The residual error of the S-parameter due to the noise is examined to appear as a complex Gaussian quotient. The statistical analysis of the residual error is given and relevant statistical quantities are derived and discussed. Experiments were conducted on a two-port VNA to validate the noise-influenced S-parameter model. We show that the uncertainty due to the noise is often critical in S-parameter measurements, in particular for S-parameters of a small magnitude.

**Index Terms**—Network analysis, noise, probability distribution, random variable, scattering parameter, uncertainty.

## NOMENCLATURE

$\cdot^*$	Complex conjugate of a complex variable.
$\langle \cdot \rangle$	Ensemble average (expectation value) of a random variable.
$\otimes$	Kronecker product.
$\cdot^\dagger$	Matrix conjugate transpose operator.
$\cdot^{-1}$	Matrix inversion operator.
$\cdot^\top$	Matrix transpose operator.
$\text{Arg}(\cdot)$	Argument of a complex variable.
$\mathbf{a}, \mathbf{b}$	Raw forward and backward composite waves containing both signals and noise.
$\bar{\mathbf{a}}, \bar{\mathbf{b}}$	Raw forward and backward signal waves (noiseless waves).
$\mathbf{a}^c, \mathbf{b}^c$	Corrected forward and backward composite waves.
$\mathbf{a}_s$	VNA source wave. It only contains one non-trivial entry $P_m$ , where index $m$ indicates the excitation port.
$\tilde{a}_{nm}$	Random variable in the denominator of $\delta\tilde{S}_{m'm}$ . Also simplified as $\tilde{a}_n$ .
$\alpha$	Wave measured by VNA reference (forward) receivers. Its $m$ -th element is $\alpha_m$ .
$\tilde{\alpha}_n$	Noise wave due to the detector noise in VNA reference receivers and its $m$ -th element is $\tilde{\alpha}_{nm}$ .
$\tilde{b}_{nm'}$	Random variable in the numerator of $\delta\tilde{S}_{m'm}$ . Also simplified as $\tilde{b}_n$ .
$\beta$	Wave measured by VNA test-port (backward) receivers. Its $m'$ -th element is $\beta_{m'}$ .

$\tilde{\beta}_n$	Noise wave due to the detector noise in VNA test-port receivers and its $m$ -th element is $\tilde{\beta}_{nm}$ .
$C(\cdot)$	Joint cumulative density function (copula) of random variables.
$\mathcal{CN}$	Complex normal distribution.
$\tilde{\mathbf{d}}_n$	Noise wave associated with a multiport network and its $m$ -th element is $\tilde{d}_{nm}$ .
$\text{diag}(\cdot)$	Diagonalization operator that produces a diagonal matrix from a column vector.
$\delta\tilde{S}_{m'm}$	Residual error of $\tilde{S}_{m'm}$ due to noise in VNA measurements. Also simplified as $\delta\tilde{S}$ and expanded as $x + jy$ .
$\text{Ei}(\cdot)$	Exponential integral function.
$\hat{\mathbf{e}}_i$	$i$ -th Cartesian base, equivalent to a column vector with one unit entry at the $i$ -th position $[0, 0, \dots, 0, 1, 0, \dots, 0]^\top$ .
$\eta$	Ratio of RMS noise determined by $\sigma_b/\sigma_a$ .
$f(\cdot)$	Probability density function of a random variable.
$F(\cdot)$	Cumulative density function of a random variable.
$\Gamma_{sm}$	Reflection coefficient of the VNA stimulus inside Port $m$ .
$\Gamma_l$	Reflection coefficient of the VNA termination inside Port $l$ .
$\Gamma$	VNA internal reflection coefficients. Its elements are either $\Gamma_{sm}$ or $\Gamma_l$ .
$\tilde{\gamma}_n$	Noise wave emanating from internal VNA sources or terminations. Its elements are either $\tilde{s}_{nm}$ or $\tilde{t}_{nl}$ .
$h(\cdot)$	Normalization coefficient of the Phi-Square test.
$\mathbf{I}$	Identity matrix.
$I_\nu(\cdot)$	Modified Bessel function of the first kind at the order of $\nu$ .
$\mathcal{J}\left(\frac{\cdot}{\cdot}\right)$	Jacobian determinant.
$j$	Imaginary unit.
$L_\nu(\cdot)$	Laguerre polynomial of degree $\nu$ .
$\max(\cdot, \cdot)$	Maximum operator.
$\mathcal{N}$	Normal distribution.
$\mathcal{O}(\cdot)$	On the same order of.
$P_m$	RMS amplitude of the VNA stimulus applied to Port $m$ . Also simplified as $P$ .
$\Phi^2$	Output of the Phi-Square test for checking mutual independence among random variables.
$\Pi(\cdot)$	Product of the individual CDF of random variables.
$\Re, \Im$	Real and imaginary part of a complex number.

D. Gu, J. Jargon and M. Ryan are with the RF Technology Division, National Institute of Standards and Technology, Boulder, CO 80305 USA (e-mail: dazhen.gu@nist.gov).

M. Ryan is also with the Department of Aerospace Engineering Sciences, University of Colorado, Boulder, Colorado 80309, USA (e-mail: matthew.j.ryan@colorado.edu).

A. Hubrechsens is with the Eindhoven University of Technology, Netherlands (e-mail: a.hubrechsens@tue.nl).

Manuscript received XXXX XX, 2020.

$\mathbb{R}^D$	Real-coordinate space with a dimension of $D$ .
$\bar{\mathbf{S}}$	Noiseless raw S-parameters associated with the external DUT cascaded by the VNA error boxes. Its $m'$ -th element is $\bar{S}_{m'm}$ .
$\bar{\mathbf{S}}^c$	Corrected S-parameters of the external DUT.
$\tilde{S}_{m'm}$	Measured S-parameter by taking ratio between $\beta_{m'}$ and $\alpha_m$ .
$\mathcal{S}, \mathcal{S}'$	Signal to noise ratio. $\mathcal{S} = P^2/\sigma_a^2$ and $\mathcal{S}' = P^2/\sigma_b^2$ .
$\tilde{s}_{nm}$	Noise wave of the VNA stimulus due to signal impurity inside Port $m$ .
$\Sigma$	Covariance matrix of a random vector.
$\sigma_a$	RMS value of $\tilde{a}_n$ .
$\sigma_b$	RMS value of $\tilde{b}_n$ .
$\mathbf{T}$	Transfer matrix. It can be partitioned to block matrices; $\mathbf{T}_{11}$ , $\mathbf{T}_{12}$ , $\mathbf{T}_{21}$ , and $\mathbf{T}_{22}$ .
$\tilde{t}_{nl}$	Noise wave of VNA termination due to passive radiation inside Port $l$ .
$V_{ij}$	Empirical probability density of a real random variable at $v_{ij}$ .
$\mathbf{v}$	Real random vector. It represents one observation of random variables of interest in practice.
$\text{vec}(\cdot)$	Matrix vectorization operator. All columns are concatenated in order to form a one-column vector.
$z$	Modulus of the residual error $\delta\tilde{S}$ .

## I. INTRODUCTION

**S**CATTERING-parameters (S-parameter) are widely used physical quantities that describe the signal-dissipation (or signal-amplification) and phase-delay characteristics of a component, particularly at radio and microwave frequencies. They are often measured on a vector network analyzer (VNA) and represented by complex numbers. A stimulus wave is sent by the VNA as a probing signal to a device under test (DUT). The signals reflected by and transmitted through the DUT are then measured on the VNA receivers. The reflected and transmitted signals, along with the original probing signal, are used for computing the S-parameters of the DUT.

Prior to the measurements of the DUT, calibrations are performed to account for the imperfections of the internal components in the instrument and the external test fixtures. Measurement uncertainties are mainly due to the uncertainty of the calibration standards, such as the variance of their physical dimensions. However, the impact of noise on the S-parameter measurements has rarely been systematically investigated except very limited modeling by Rytting [1] and Garelli [2]. Electronic noise is a manifestation of ubiquitous random processes in any system. For S-parameter measurements, there is noise present in the stimulus sources and the receivers inside the VNA. In addition, external DUTs, regardless of being passive or active, introduce extra noise into the signal detection. Both Rytting and Garelli modeled the effect of noise on all the waves in two parts; a multiplicative term and an additive term [1], [2]. Neither model accounts for the physical origins of the noise. More recently, Marinov proposed a model that includes noise in the generator and the receiver for one-port reflection

measurements [3]. Several experiment studies showed that the signal-to-noise ratio (SNR) was crucial for predicting the influence of noise on S-parameter measurements performed by the VNA and the reflectometer [3]. In active load-pull systems, Nopchinda *et. al.* modeled the noise contributions to the VNA waves solely due to the receiver impairments [4]. Some accuracy improvements were demonstrated in measuring reflection and transmission coefficients [4]. Nevertheless, a comprehensive picture to account for multiple noise origins in S-parameter measurements is not available to date.

When SNR is high, the influence of noise may be minimal and can be safely neglected if uncertainties of other dominating factors are included in the analysis. However, the influence of noise becomes pronounced when SNR is low. For example, a scattered “cloud” of S-parameter data centered at its noiseless mean value are commonly encountered during measurements. Even when SNR is high, the uncertainty due to the noise may be critical if the S-parameter magnitude of the DUT is very small, e.g. reflection off a highly absorptive device and transmission through a highly dissipative attenuator. Customarily, we make redundant measurements in order to average out the noise. However, some fundamental concerns remain; can we predict the magnitude of the spread of the S-parameters, how do we account for the uncertainty due to the noise, what is the tolerance interval associated with such variation? This paper aims to answer these concerns.

In this paper, we develop an analytical model and derive an expression for the noise-induced residual error in the complex S-parameters, as presented in Section II. Next, we analyze the residual error from the statistical perspective in Section III. Section IV extends the uncertainty analysis for the corrected S-parameters. Various experiments verify the noise model and show the importance of the noise-related uncertainty under certain circumstances in Section V. In the end, results were discussed and the conclusion was drawn in Sections VI and VII.

## II. MODEL OF S-PARAMETER MEASUREMENT WITH NOISE

Similar to the noise analysis of multiport amplifiers [5], we consider a linear multiport configuration with the port number equal to  $M$  as shown in Fig. 1. At this point, the VNA error terms are yet to be corrected. The error boxes for each port are marked in red in Fig. 1 and they are lumped together with the external DUT. As such, the  $M$ -port network consists of both the external DUT and internal VNA error boxes. In the following analysis, all the waves are uncorrected raw waves. We will address the error corrections and uncertainty propagation in Section IV.

In addition to the noiseless waves  $\bar{\mathbf{a}}$  and  $\bar{\mathbf{b}}$  (not shown in the figure), the *effective* noise waves  $\tilde{\mathbf{d}}_n$ ,  $\tilde{\alpha}_n$ ,  $\tilde{\beta}_n$  and  $\tilde{\gamma}_n$  (i.e.,  $\tilde{s}_{nm}$  and  $\tilde{t}_{nl}$ ) are injected into various stages of the signal path. As a consequence, all the components can now be regarded noiseless. Here,  $\bar{\mathbf{a}}$ ,  $\bar{\mathbf{b}}$ ,  $\tilde{\mathbf{d}}_n$ ,  $\tilde{\alpha}_n$ ,  $\tilde{\beta}_n$  and  $\tilde{\gamma}_n$  are all  $M \times 1$  column vectors. Aside from the noise contributed by the  $M$ -port network ( $\tilde{\mathbf{d}}_n$ ), the new model consists of two primary differences from the previous model [5]. 1) The noise due to

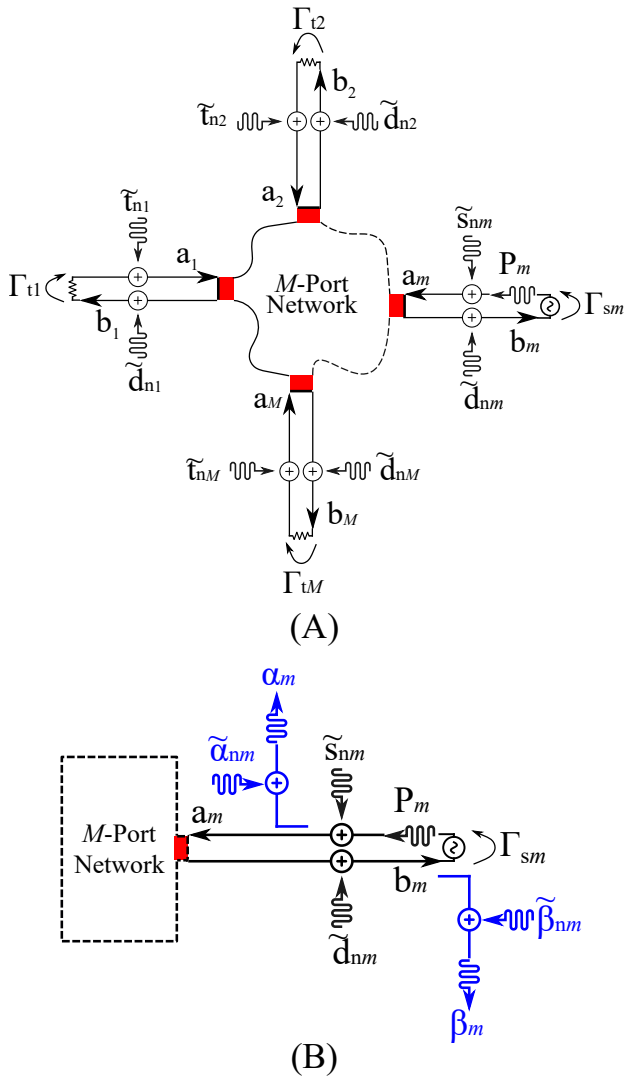


Fig. 1. (A) An arbitrary  $M$ -port network measured by a VNA. The network consists of both external DUT and internal error boxes marked in red. Port  $m$  is the exciting or stimulus port and the other ports are in the receiving mode. Note that the receiver noise is not included for graphical clarity. (B) Sketch of Port  $m$  with additional components related to forward- (reference) and backward-wave (test-port) receivers marked in blue.

either the VNA stimulus or internal terminations, designated by  $\tilde{\gamma}_n$ , is accounted for in the model. 2) Also included are the noise components ascribed to the VNA receivers, denoted by  $\tilde{\alpha}_n$  and  $\tilde{\beta}_n$ .

We elaborate on the four noise waves as follows.

- 1) Noise  $\tilde{d}_{nm}$ , emanating from Port  $m$  of the  $M$ -port network, propagates towards the VNA internal terminations or sources. It is either due to passive radiation or active electronics intrinsic to the  $M$ -port network. All elements of  $\tilde{\mathbf{d}}_n$  are emerging waves with respect to the  $M$ -port network.
- 2) Elements  $\tilde{\alpha}_{nm}$  and  $\tilde{\beta}_{nm}$  are associated with detection noise of the reference and test-port VNA receivers inside Port  $m$ . The reference receivers measure the wave as it goes out of the VNA, while the test-port receivers measure the wave as it comes into the VNA. All these noise waves are only present in the corresponding

receivers. Note that none of  $\tilde{\alpha}_n$  is injected into the  $M$ -port network.

- 3) Noise wave  $\tilde{\gamma}_n$  has implicit dependence on which port of the VNA excites a stimulus signal. For S-parameter measurements, one of the VNA ports is in the excitation mode at a time and the rest are in the receiving mode. If Port  $m$  is in the excitation mode, a pure stimulus signal  $P_m$  is generated along with the noise  $\tilde{s}_{nm}$  due to the signal impurity. The stimulus signal is a sinusoidal wave with an amplitude of  $\sqrt{2}P_m$  at the frequency of interest:  $\sqrt{2}P_m \cos(2\pi ft)$ . Each of the other  $(M - 1)$  ports is internally terminated with a load and all of them act in the receiving mode. There are noise waves,  $\tilde{t}_{nl}$  ( $l = 1$  to  $M$  and  $l \neq m$ ), emanating from these loads due to the passive radiation. In the vector format, the source signal  $\mathbf{a}_s(m)$  and the associated noise  $\tilde{\gamma}_n(m)$  can be expressed by

$$\mathbf{a}_s(m) = [0, 0, \dots, P_m, \dots, 0]^\top, \quad (1a)$$

$$\tilde{\gamma}_n(m) = [\tilde{t}_{n1}, \tilde{t}_{n2}, \dots, \tilde{s}_{nm}, \dots, \tilde{t}_{nM}]^\top, \quad (1b)$$

Noise in different noise waves is considered independent from each other except that correlations may exist among individual elements of  $\tilde{\mathbf{d}}_n$ . For a passive  $M$ -port network, the correlation is deterministic and relates to its S-parameters [6]. Furthermore, each noise wave is a complex quantity. Its real and imaginary parts represent, respectively, the inphase and quadrature components of the noise signal at the frequency of interest. For the narrow-band noise signal, the real and imaginary parts can be regarded as independent and identically distributed (i.i.d.) random variables (RVs) [7]. This fact is implicitly used in the modeling and the statistical analysis throughout the paper.

For an  $M$ -port network with Port  $m$  in the excitation mode, the wave quantities are governed by

$$\mathbf{b} = \bar{\mathbf{S}}\mathbf{a} + \tilde{\mathbf{d}}_n, \quad (2a)$$

$$\mathbf{a} = \mathbf{\Gamma}\mathbf{b} + \mathbf{a}_s(m) + \tilde{\gamma}_n(m), \quad (2b)$$

where  $\bar{\mathbf{S}}$  is the true S-parameters of the network.  $\bar{\mathbf{S}}$  should be the measured raw S-parameters in the absence of noise. For the sake of generality, we also include a diagonal  $M \times M$  matrix  $\mathbf{\Gamma}$  to account for the imperfect matches of the VNA source and terminations, although the magnitude of the elements in  $\mathbf{\Gamma}$  is small in modern VNA instruments. The  $\mathbf{\Gamma}$  matrix can be expressed as

$$\mathbf{\Gamma} = \text{diag}([\Gamma_{t1}, \Gamma_{t2}, \dots, \Gamma_{sm}, \dots, \Gamma_{tM}]^\top), \quad (3)$$

where  $\Gamma_t$  variables are the reflection coefficients of VNA terminations and  $\Gamma_{sm}$  is the reflection coefficient of the stimulus in Port  $m$ . It can be shown that the outgoing wave  $\mathbf{a}$  is

$$\begin{aligned} \mathbf{a} &= (\mathbf{I} - \mathbf{\Gamma}\bar{\mathbf{S}})^{-1} (\mathbf{a}_s + \tilde{\gamma}_n + \mathbf{\Gamma}\tilde{\mathbf{d}}_n) \\ &= (\mathbf{I} - \mathbf{\Gamma}\bar{\mathbf{S}})^{-1} \mathbf{a}_s + \tilde{\gamma}_n + \mathcal{O}(|\mathbf{\Gamma}\tilde{\gamma}_n|, |\mathbf{\Gamma}\tilde{\mathbf{d}}_n|) \\ &\approx (\mathbf{I} - \mathbf{\Gamma}\bar{\mathbf{S}})^{-1} \mathbf{a}_s + \tilde{\gamma}_n. \end{aligned} \quad (4)$$

The approximation is made to the first order of the magnitude of  $\mathbf{\Gamma}$  and the root-mean-square (RMS) magnitude of the

noise wave, since both of them are small quantities. With substitution of  $\mathbf{a}$  in (4) into (2a), the incoming wave  $\mathbf{b}$  can be expressed by

$$\mathbf{b} = \bar{\mathbf{S}} \left[ (\mathbf{I} - \Gamma \bar{\mathbf{S}})^{-1} \mathbf{a}_s + \tilde{\gamma}_n \right] + \tilde{\mathbf{d}}_n \quad (5)$$

Extending to the waves measured by VNA receivers with consideration of noise in the detectors as shown in Fig. 1(B), we have

$$\boldsymbol{\alpha} = \mathbf{a} + \tilde{\boldsymbol{\alpha}}_n, \quad (6a)$$

$$\boldsymbol{\beta} = \mathbf{b} + \tilde{\boldsymbol{\beta}}_n. \quad (6b)$$

All  $\alpha$ 's are referred to as reference receivers and all  $\beta$ 's are referred to as test-port receivers. We want to point out that the total noise measured by the receiver contains not only the detection noise intrinsic to the receiver but also the noise already presented in the measured waves. This is implicitly shown in (6a) and (6b).

Under the noiseless conditions,  $\mathbf{a}$  and  $\boldsymbol{\alpha}$  reduce to  $\bar{\mathbf{a}}$ , and  $\mathbf{b}$  and  $\boldsymbol{\beta}$  reduce to  $\bar{\mathbf{b}}$ . Substitution of (4) and (5) to (6a) and (6b) leads to

$$\boldsymbol{\alpha} = (\mathbf{I} - \Gamma \bar{\mathbf{S}})^{-1} \mathbf{a}_s + \tilde{\gamma}_n + \tilde{\boldsymbol{\alpha}}_n, \quad (7a)$$

$$\boldsymbol{\beta} = \bar{\mathbf{S}} (\mathbf{I} - \Gamma \bar{\mathbf{S}})^{-1} \mathbf{a}_s + \tilde{\mathbf{d}}_n + \tilde{\boldsymbol{\beta}}_n + \bar{\mathbf{S}} \tilde{\gamma}_n, \quad (7b)$$

Most of the noise terms in (7a) and (7b) are fairly intuitive. The last term in (7b) are those noise waves associated with the VNA stimulus or internal terminations. They propagate toward the  $M$ -port network and are eventually coupled to each test-port receiver; *i.e.*  $\boldsymbol{\beta}$ . For Port  $m'$ , the coupling coefficient of each element in (1b) is  $\bar{S}_{m'l}$  with  $l = 1$  to  $M$ .

In view of (1a), (1b), (7a) and (7b), the noisy S-parameters measured by the VNA are

$$\begin{aligned} \tilde{S}_{m'm} &= \frac{\beta_{m'}}{\alpha_m} \\ &= \bar{S}_{m'm} + \frac{\sum_{\substack{l=1 \\ l \neq m}}^M \bar{S}_{m'l} \left[ (\mathbf{I} - \Gamma \bar{\mathbf{S}})^{-1} \right]_{lm}}{\left[ (\mathbf{I} - \Gamma \bar{\mathbf{S}})^{-1} \right]_{mm} + \frac{\tilde{s}_{nm} + \tilde{\alpha}_{nm}}{P_m}} + \delta S_{m'm}. \end{aligned} \quad (8)$$

The detailed derivation can be found in Appendix A. The first term is the raw S-parameter of the  $M$ -port DUT embedded in the VNA error boxes. Aside from an SNR-related fraction, the second term is due to the imperfect VNA internal terminations. It can be taken care of by the so-called "switch-term" correction during the VNA calibration [1], [8]. The third term  $\delta S_{m'm}$  is the noise contribution to the S-parameters. It is the focus of this investigation. The noise-induced residual error is

$$\begin{aligned} \delta S_{m'm} &= \frac{\tilde{b}_{nm'}}{\left[ (\mathbf{I} - \Gamma \bar{\mathbf{S}})^{-1} \right]_{mm} P_m + \tilde{a}_{nm}} \\ &\approx \frac{\tilde{b}_{nm'}}{P_m + \tilde{a}_{nm}}, \end{aligned} \quad (9)$$

where shorthanded notations  $\tilde{a}_{nm}$  and  $\tilde{b}_{nm'}$  are used. They are given by

$$\tilde{a}_{nm} = \tilde{s}_{nm} + \tilde{\alpha}_{nm}, \quad (10a)$$

$$\tilde{b}_{nm'} = \tilde{d}_{nm'} + \tilde{\beta}_{nm'} - \bar{S}_{m'm} \tilde{\alpha}_{nm} + \sum_{\substack{l=1 \\ l \neq m}}^M \bar{S}_{m'l} \tilde{t}_{nl}. \quad (10b)$$

In addition, an approximation is made in (9) to neglect the VNA source reflection. This is reasonable considering the VNA generator (possibly in combination with isolators) is typically well matched. Nevertheless, the following statistical analysis should still be applicable if the approximation is not made. After all, the approximated scaling factor only insignificantly changes the stimulus strength  $P_m$ .

Evidently, the numerator of  $\delta S_{m'm}$  is a linear combination of  $(M+2)$  independent RVs while the denominator contains a static quantity and two linearly combined independent RVs. By use of the identities of independence and zero means, the following expressions of the variances can be deduced.

$$\begin{aligned} \sigma_a^2 &= \langle \tilde{a}_{nm} \tilde{a}_{nm}^* \rangle \\ &= \langle |\tilde{s}_{nm}|^2 \rangle + \langle |\tilde{\alpha}_{nm}|^2 \rangle, \end{aligned} \quad (11a)$$

$$\begin{aligned} \sigma_b^2 &= \langle \tilde{b}_{nm'} \tilde{b}_{nm'}^* \rangle \\ &= \langle |\tilde{d}_{nm'}|^2 \rangle + \langle |\tilde{\beta}_{nm'}|^2 \rangle \\ &\quad + |\bar{S}_{m'm}|^2 \langle |\tilde{\alpha}_{nm}|^2 \rangle + \sum_{\substack{l=1 \\ l \neq m}}^M |\bar{S}_{m'l}|^2 \langle |\tilde{t}_{nl}|^2 \rangle. \end{aligned} \quad (11b)$$

Although  $\tilde{a}_{nm}$  and  $\tilde{b}_{nm}$  correlate through the term  $\tilde{\alpha}_{nm}$ , we consider the correlation is approximately negligible. Therefore  $\tilde{a}_{nm}$  and  $\tilde{b}_{nm}$  are independent RVs, since two uncorrelated normally distributed RVs are independent. This approximation will be validated in Section V, where most of experimental data showed that the reference receiver noise was much lower than either the noise in stimulus signal or the noise in the test-port receiver. This manipulation also simplifies the statistical analysis in Section III.

We have now established the model of S-parameter measurements subject to noisy conditions. The noise-induced residual error manifests as a quotient containing various complex RVs. Next, we can proceed to analyze how noise affects the measurements from a statistics standpoint.

### III. STATISTICS OF NOISY S-PARAMETERS

The goal is to investigate the statistical properties of the complex quantity  $\delta S$  given in (9). A clear understanding of the statistics of the residual error  $\delta S$  allows us to evaluate the measurement uncertainty associated with noise and the corresponding tolerance intervals. In addition, it provides the theoretical basis for how the residual error caused by noise is statistically distributed; under what conditions it can be considered a normal distribution.

All the noise appearing in Section II corresponds to a random stationary process. We only require wide-sense stationarity, namely the mean and the auto-covariance of the random process are invariant of time. More specifically, the mean of the noise waves is zero and the variance of the noise waves is constant, equivalent to the power of a band-limited noise centered at the frequency of interest. Furthermore, any finite samples of measured noise waves are normally distributed.

We now suppress the port index of  $\delta S$  and other variables for brevity in this section. RVs  $\tilde{a}_n$  and  $\tilde{b}_n$  represent independent narrow-band noise signals within the IF bandwidth set by the VNA. Their individual components are shown in (10a) and (10b). Both can be modeled as complex Gaussian RVs with circular symmetry, denoted by  $\mathcal{CN}$ .

The RV in the numerator of (9) follows  $\mathcal{CN}(0, \sigma_b^2)$ , where  $\sigma_b^2$  is equivalent to the noise power of wave  $b_n$  within the bandwidth. The mean of the RV on the denominator is a non-zero number  $P$ . In general,  $P$  is a complex quantity that represents the inphase and quadrature components of the stimulus signal. Since the phase is a relative quantity,  $P$  can be set to be real and positive. Therefore,  $P$  corresponds to the RMS amplitude of the sine wave produced by the VNA generator at the frequency of interest<sup>1</sup>. The entire denominator can be viewed as an RV following  $\mathcal{CN}(P, \sigma_a^2)$ . This is a well studied subject largely due to Rice [9].

Direct computation of the probability distribution function (PDF) of the real and imaginary parts of  $\delta S$  is prohibitively complicated. We take a detour to study the PDF of its magnitude and phase first. In what follows, we present the statistical analysis in a relatively succinct way. The detailed derivation was documented in [10].

#### A. PDF of $|\delta S|$

To facilitate the formulation, we normalize the RVs as follows,

$$r_1 = \left| \frac{P + \tilde{a}_n}{\sigma_a/\sqrt{2}} \right|, \quad (12a)$$

$$r_2 = \left| \frac{\tilde{b}_n}{\sigma_b/\sqrt{2}} \right|. \quad (12b)$$

So that  $r_1$  follows the Rice (Nakagami-n) distribution of unit noise power and  $r_2$  follows the Rayleigh distribution of unit mode. Their PDFs can be expressed by

$$f_{R_1}(r_1) = r_1 \exp\left(-\frac{r_1^2 + 2\mathcal{S}}{2}\right) I_0\left(\sqrt{2\mathcal{S}}r_1\right), \quad (13a)$$

$$f_{R_2}(r_2) = r_2 \exp\left(-\frac{r_2^2}{2}\right). \quad (13b)$$

Both  $r_1$  and  $r_2$  are in the domain of  $[0, +\infty)$ . Otherwise, the PDFs of  $r_1$  and  $r_2$  are zero.  $\mathcal{S}$  symbolizes the SNR, namely  $P^2/\sigma_a^2$ .

We define the ratio of these two RVs as  $\hat{z} \equiv r_2/r_1$ . As such, the modulus of  $\delta S$ , designated as  $z \equiv |\delta S|$ , is simply a scaled variant of  $\hat{z}$ , given by  $\eta\hat{z}$ . Here the ratio of the RMSed noise waves is  $\eta \equiv \sigma_b/\sigma_a$ . To determine the PDF of  $z$ , we can start by finding the PDF of  $\hat{z}$ , followed by a change of the variable. The PDF  $f_{\hat{z}}$  can be obtained by first computing the the cumulative distribution function (CDF)  $F_{\hat{z}}(\hat{z} < \hat{z}_0)$ . The

<sup>1</sup>We adopt the power wave notation to match the experimental data. Therefore, all the wave quantities implicitly contain a normalization constant related to the system impedance. In this case, this constant is  $1/\sqrt{50}$ .

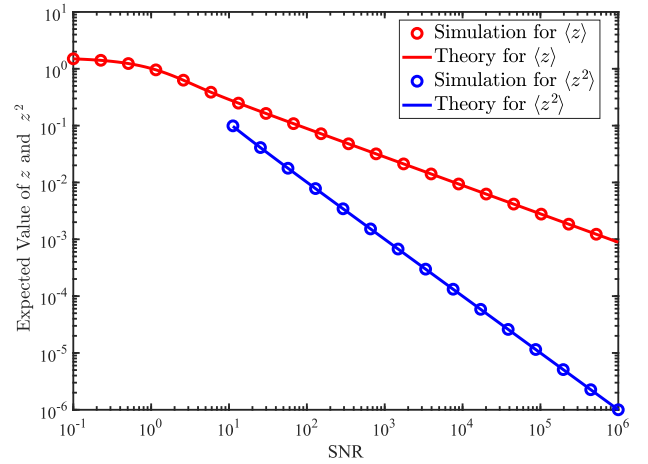


Fig. 2. Expected values of  $z$  (red) and  $z^2$  (blue) for  $\eta = 1$ . Under the medium and high SNR,  $\langle z \rangle$  and  $\langle z^2 \rangle$  linearly reduce with the SNR on the logarithmic scale. The slopes are  $-0.5$  and  $-1$ , respectively.

independence between these two RVs allows us to calculate the CDF as

$$F_{\hat{z}}(\hat{z} < \hat{z}_0) = \int_0^{+\infty} dr_1 f_{R_1}(r_1) \int_0^{r_1 \hat{z}_0} dr_2 f_{R_2}(r_2). \quad (14)$$

Next, the derivative with respect to  $\hat{z}_0$  is applied to the CDF. After lengthy algebraic steps, we reach

$$f_Z(z) = \frac{2ze^{-\mathcal{S}}(1 + \mathcal{S} + z^2/\eta^2)}{\eta^2(1 + z^2/\eta^2)^3} \exp\left(\frac{\mathcal{S}}{1 + z^2/\eta^2}\right). \quad (15)$$

Once again, the PDF in (15) is valid for  $z \in [0, +\infty)$ . The PDF vanishes for negative  $z$ .

#### B. First Moment of $f_Z(z)$

The first moment (or the mean) is naturally the very first parameter that warrants a close look. It can be used to compare with the experimental data to validate the model. For example, the mean of the radius of the noisy S-parameter can be obtained from the measured data. It characterizes how big the noise-induced spread in S-parameter measurements on a Smith chart. Furthermore, other statistical properties can be inferred from the first moment.

With its PDF available from (15), the mean of  $z$  can be calculated directly from

$$\langle z \rangle = \int_0^{+\infty} z f_Z(z) dz. \quad (16)$$

The integration is not straightforward. A feasible approach is to first expand the exponential function into a power series. Next, the summation and the integral can be switched in order, which in turn enables closed-form solutions to each integration term. Finally, the series of integrated expressions are summed to arrive at the end result. The first moment turns out to be the closed-form expression

$$\langle z \rangle = \eta \frac{\pi I_0(\mathcal{S}/2)}{2e^{\mathcal{S}/2}}, \quad (17)$$

where  $\eta = \sigma_b/\sigma_a$ .

The asymptotic expressions of  $\langle z \rangle$  are also of interest, not only for ease of numerical calculations, but also for prediction of its behavior at high SNR and low SNR limits. By use of Hankel's expansions of the modified Bessel functions [11], it can be shown at a high SNR

$$\lim_{S \rightarrow \infty} \langle z \rangle = \frac{\eta}{2} \sqrt{\frac{\pi}{S}} + \mathcal{O}\left(\frac{1}{\sqrt{S^3}}\right). \quad (18)$$

By inspection of its original form in (9),  $\delta S$  acts like a complex RV with its PDF approximate to  $\mathcal{CN}(0, \sigma_b^2/P^2)$  at a high SNR. The mean of the modulus of such a variate is  $\sqrt{\pi/2} \cdot [\sigma_b/(\sqrt{2}P)]$ , which agrees with the result above. This indicates that the spread of S-parameters at a high SNR scales with the square root of the noise-to-signal ratio (NSR). For example, the expected radius of the S-parameter spread is roughly 0.001 at 60 dB SNR.

With Taylor's expansion of the modified Bessel functions, the limit at low SNR can be found as

$$\lim_{S \rightarrow 0} \langle z \rangle = \eta \frac{\pi}{2} + \mathcal{O}(S). \quad (19)$$

As the signal power becomes negligible to the noise power,  $\delta S$  resembles the quotient of two complex RVs that independently follow  $\mathcal{CN}(0, \sigma_b^2)$  and  $\mathcal{CN}(0, \sigma_a^2)$ . As a consequence, the magnitude of the quotient converges to the ratio of two Rayleigh RVs with scalar parameters of  $\sigma_a$  and  $\sigma_b$  respectively. This tells us that the expected radius approaches a constant level at about 1.57 times the ratio of the RMSed noise waves.

Direct use of (17) is infeasible for prediction, especially at SNRs above 30 dB where the large arguments lead to difficulties in evaluations of the modified Bessel function and the exponential function. At low and high SNR limits, we resort to (18) and (19) instead.

We used Monte Carlo simulation to generate a large number of samples of complex random variables that follow the distribution  $\mathcal{CN}(0, 2)$  and  $\mathcal{CN}(\sqrt{2S}, 2)$ . Next the division was taken to produce  $z$ , which in turn allowed statistical analysis, such as first and second moment computation, to be implemented on the sample. Figure 2 shows the simulation results compared with the theoretical prediction. An excellent agreement between the simulation and the prediction is reached at all SNR levels.

### C. Second Moment of $f_Z(z)$

The second moment is the value of  $\langle |\delta \tilde{S}|^2 \rangle$ . Such a quantity has applications in VNA measurements when power related quantities are of interest. For example, noise effects need to be removed in Rician K-factor measurements conducted in a reverberation chamber in order to extract the random signal reflection solely due to paddle rotations [12]. More on this topic will appear in a future publication.

The integral for calculating the second moment is also straightforward. Although the definite integral does not generally converge, an asymptotic analysis shows that the integral approaches a calculable limit under relatively high SNR conditions. The asymptote can be expressed as

$$\lim_{S \rightarrow \infty} \langle z^2 \rangle = \eta^2 \frac{\text{Ei}(S)}{e^S} = \frac{\eta^2}{S} + \mathcal{O}\left(\frac{1}{S^2}\right), \quad (20)$$

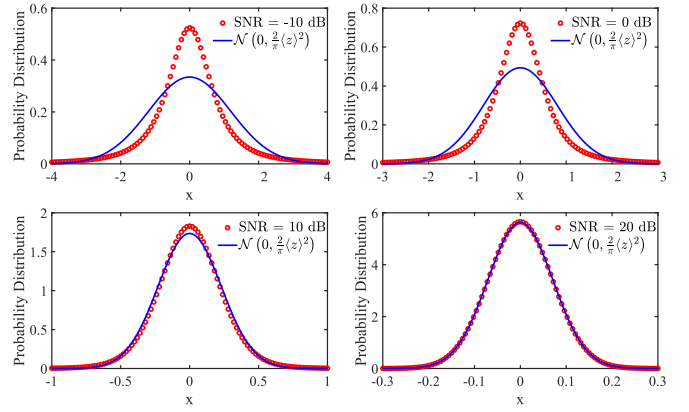


Fig. 3. PDFs of the real (or the imaginary) part of  $\delta S$  at different SNR levels; -10 dB, 0 dB, 10 dB, and 20 dB. Normal distribution following  $\mathcal{N}(0, \frac{2}{\pi} \langle z \rangle^2)$  for each case is also plotted for comparison. As the SNR increases, the distribution is approximately a normal distribution.

where Ei is the exponential integral function. This shows that, to the first order approximation, the second moment is identical to the NSR at a relatively high SNR. Note that this NSR refers to the noise power in  $b_n$  wave or  $\sigma_b^2/P^2$ .

Numerical simulations show that the high-limit approximation works very well above 20 dB SNR, as shown in Fig. 2. The agreement at 20 dB and beyond is better than 99.9%. Even at 10 dB SNR, the theoretical prediction is only off by about 2%. Note that this excellent agreement is achieved by retaining the approximation up to the second order of  $1/S$  for SNR levels below 20 dB.

The existence of the second moments at moderate and large SNR levels also allows us to calculate the variance of the RVs. We will use this finding implicitly in the covariance matrix calculations in Section IV.

### D. PDFs of Real and Imaginary Parts

In order to obtain the PDFs of  $\Re(\delta S)$  (denoted as  $x$ ) and  $\Im(\delta S)$  (denoted as  $y$ ), the PDF of the phase angle ( $f_\Theta(\theta)$ ) is also needed. It can be shown that the phase angle is uniformly distributed [10]. With  $f_Z$  and  $f_\Theta$  at our disposal, the PDF of  $x$  (or the PDF of  $y$ ) can be readily acquired from the marginal distribution of the joint PDF  $f_{XY}(x, y)$

$$\begin{aligned} f_X(x) &= \int_{-\infty}^{+\infty} f_{XY}(x, y) dy \\ &= \int_{-\infty}^{+\infty} \mathcal{J}\left(\frac{x, y}{z, \theta}\right) f_Z(z) f_\Theta(\theta) dy. \end{aligned} \quad (21)$$

Here a coordinate transformation is included to change  $z$  and  $\theta$  to  $x$  and  $y$ . The integration is an involved process and can be found in [10]. The result is

$$\begin{aligned} f_X(x) &= \frac{\exp\left(\frac{S}{2\mathcal{X}}\right)}{2\eta e^S \mathcal{X}^{3/2}} \left[ \left(1 + \frac{S}{\mathcal{X}}\right) I_0\left(\frac{S}{2\mathcal{X}}\right) \right. \\ &\quad \left. + \frac{S}{\mathcal{X}} I_1\left(\frac{S}{2\mathcal{X}}\right) \right], \end{aligned} \quad (22)$$

where  $\mathcal{X} = 1 + x^2/\eta^2$ . Note that the RVs corresponding to the real and the imaginary parts distribute identically.

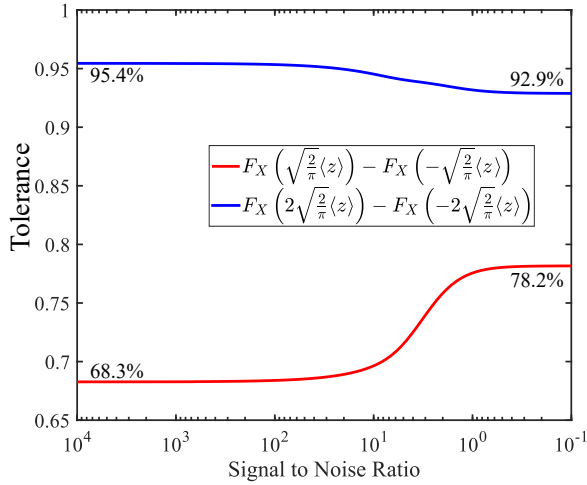


Fig. 4. Tolerance for intervals of  $[-\sqrt{\frac{2}{\pi}}\langle z \rangle, \sqrt{\frac{2}{\pi}}\langle z \rangle]$  (red) and  $[-2\sqrt{\frac{2}{\pi}}\langle z \rangle, 2\sqrt{\frac{2}{\pi}}\langle z \rangle]$  (blue). Asymptotic tolerance levels are marked at high and low SNR limits.

Not surprisingly, both  $x$  and  $y$  are symmetrically distributed about zero. Furthermore, it can be shown that the PDF in (22) approaches  $\mathcal{N}(0, 0.5/S')$  in high SNR conditions.  $S'$  is the SNR with respect to noise power in  $\tilde{b}_n$ , or  $P^2/\sigma_b^2$ . This trend is also evident from plots of the PDF as a function of SNR in Fig. 3. As the SNR increases, distribution of  $f_X(x)$  resembles more closely to a normal distribution. For lower SNR levels, the probability is more concentrated around  $x = 0$  in comparison to the normal distribution. It is also interesting to note that  $x$  and  $y$  are uncorrelated but not generally independent.

#### E. Uncertainty and Tolerance Interval

With the PDF  $f_X(x)$  available, it is ready for us to evaluate the noise-induced measurement uncertainty and the tolerance interval associated with the variability of the RV. Assuming the uncertainty of  $x$  is  $u_x$ , the probability in the range of  $[-u_x, u_x]$  can be calculated from the CDFs of  $x$  as

$$F_X(u_x) - F_X(-u_x) = 2 \int_0^{u_x} f_X(x) dx. \quad (23)$$

Unfortunately, a closed-form expression for the integral is not available. Consequently, a numerical computation is needed to solve  $u_x$  for a desired tolerance, for example 68.3% and 95.4%.

Nevertheless, a heuristic guess can be made from the analysis in Section III-B and III-D. Since  $f_X$  approaches  $\mathcal{N}(0, \frac{2}{\pi}\langle z \rangle^2)$  in high SNR limits,  $\langle z \rangle/\sqrt{\pi/2}$  may be used for the estimate of  $u_x$  across all SNR levels.

Figure 4 shows the tolerance associated with  $[-u_x, u_x]$  and  $[-2u_x, 2u_x]$  as a function of SNRs. The tolerance in the interval  $[-u_x, u_x]$  grows monotonically from about 68.3% to 78.2% as the SNR reduces. Therefore, the use of  $\langle z \rangle/\sqrt{\pi/2}$  as the uncertainty is relatively conservative across all SNRs. However, the tolerance decreases slightly from 95.5% to 92.9% for the interval  $[-2u_x, 2u_x]$ , corresponding to the expanded uncertainty with a coverage factor of 2.

In practice, the SNR in VNA measurements is rarely below 40 dB [13]. As a result, the estimate we come up with should be applicable to most VNA measurements. Nevertheless, the analysis covers low SNR conditions as long as the developed model still holds valid.

In passing,  $\bar{S} \pm \left( \sqrt{\frac{1}{2S'}} + j\sqrt{\frac{1}{2S'}} \right)$  and  $\bar{S} \pm \left( \sqrt{\frac{2}{S'}} + j\sqrt{\frac{2}{S'}} \right)$  represent 68.3% and 95.5% tolerance intervals respectively due to the noise in ordinary S-parameter measurements. Uncertainties between the real and imaginary parts are uncorrelated. In other words,  $\delta S$  remains a circularly symmetric Gaussian RV  $\sim \mathcal{CN}(0, 1/S')$  under moderate and high SNR conditions.

#### IV. UNCERTAINTY PROPAGATION

We have so far formulated the noise-induced uncertainty of the uncorrected S-parameter. This uncertainty is associated with the raw S-parameter of the DUT cascaded with the VNA error boxes. We now turn our attention to how to propagate uncertainty to the corrected S-parameter  $\bar{\mathbf{S}}^c$  pertaining solely to the DUT. Since it is independent from other uncertainty sources, e.g. those due to dimensional uncertainties in calibration standards, the uncertainty due to noise can be propagated independently.

For propagating the uncertainty, we need to obtain the covariance matrix of the uncorrected S-parameters. From its original form of a  $M \times M$  matrix,  $\delta \mathbf{S}$  first needs to be vectorized by concatenating its columns in order.

$$\text{vec}(\delta \mathbf{S}) = [\delta S_{11}, \dots, \delta S_{M1}, \delta S_{12}, \dots, \delta S_{MM}]^\top. \quad (24)$$

Each element in  $\text{vec}(\delta \mathbf{S})$  contains real and imaginary parts, equivalent to  $2M^2$  error terms. In general, we would have to obtain the covariance of each pair of  $2M^2$  variables. This leads to a total  $4M^4$  pairs. However, a simplified notation can be implemented for these RVs under certain circumstances. As noted in the last section,  $\delta S_{m'm}$  is a Gaussian RV with circular symmetry for ordinary VNA measurements when the SNR is relatively high. It can be further shown that  $\text{vec}(\delta \mathbf{S})$  is a circularly-symmetric Gaussian random vector. Consequently, the covariance of  $4M^4$  scalar RV pairs has a unique structure. Their covariance values can be entirely determined by the  $M^4$  complex elements in the covariance matrix of the complex random vector, i.e.  $\Sigma_{\text{vec}(\delta \mathbf{S})}$ . This unique relation can be expressed by

$$\Sigma_{[\Re(\text{vec}^\top(\delta \mathbf{S})), \Im(\text{vec}^\top(\delta \mathbf{S}))]^\top} = \frac{1}{2} \begin{bmatrix} \Re(\Sigma_{\text{vec}(\delta \mathbf{S})}) & -\Im(\Sigma_{\text{vec}(\delta \mathbf{S})}) \\ \Im(\Sigma_{\text{vec}(\delta \mathbf{S})}) & \Re(\Sigma_{\text{vec}(\delta \mathbf{S})}) \end{bmatrix}. \quad (25)$$

This identity enables us to simply focus on the covariance of the complex RVs. Under moderate and large SNR conditions, the covariance matrix  $\Sigma_{\text{vec}(\delta \mathbf{S})}$  can be expressed in block matrix format as

$$\Sigma_{\text{vec}(\delta \mathbf{S})} = \begin{bmatrix} \frac{\Sigma_{\tilde{b}_{11}}}{P_1^2} & \frac{\Sigma_{\tilde{b}_{12}}}{P_1 P_2} & \dots & \frac{\Sigma_{\tilde{b}_{1M}}}{P_1 P_M} \\ \frac{\Sigma_{\tilde{b}_{21}}}{P_2 P_1} & \frac{\Sigma_{\tilde{b}_{22}}}{P_2^2} & \dots & \frac{\Sigma_{\tilde{b}_{2M}}}{P_2 P_M} \\ \vdots & \vdots & \ddots & \vdots \\ \frac{\Sigma_{\tilde{b}_{M1}}}{P_M P_1} & \frac{\Sigma_{\tilde{b}_{M2}}}{P_M P_2} & \dots & \frac{\Sigma_{\tilde{b}_{MM}}}{P_M^2} \end{bmatrix}. \quad (26)$$

TABLE I  
VNA WAVE ESTIMATION AND CORRESPONDING MODEL PARAMETERS

Processed VNA Waves	Physical Components
$\langle  \alpha_1(1) ^2 \rangle$	$P_1^2 + \langle  \tilde{s}_{n1} ^2 \rangle + \langle  \tilde{\alpha}_{n1} ^2 \rangle$
$\langle  \alpha_1(1) ^2 \rangle^2$	$P_1^2$
$\langle  \alpha_2(1) ^2 \rangle$	$\langle  \tilde{\alpha}_{n2} ^2 \rangle + \langle  \tilde{t}_{n2} ^2 \rangle$
$\langle  \beta_2(1) ^2 \rangle$	$\langle  \tilde{\beta}_{n2} ^2 \rangle + k_B T_0 \Delta f$
$\langle  \alpha_1(2) ^2 \rangle$	$\langle  \tilde{\alpha}_{n1} ^2 \rangle + \langle  \tilde{t}_{n1} ^2 \rangle$
$\langle  \beta_1(2) ^2 \rangle$	$\langle  \tilde{\beta}_{n1} ^2 \rangle + k_B T_0 \Delta f$
$\langle  \alpha_2(2) ^2 \rangle$	$P_2^2 + \langle  \tilde{s}_{n2} ^2 \rangle + \langle  \tilde{\alpha}_{n2} ^2 \rangle$
$\langle  \alpha_2(2) ^2 \rangle^2$	$P_2^2$

Here  $\Sigma_{\tilde{b}_{ij}}$  in each cell is a  $M \times M$  matrix given by

$$\begin{aligned} \Sigma_{\tilde{b}_{ij}} = & \Sigma_{\tilde{d}} + \Sigma_{\tilde{\beta}} + \tilde{\mathbf{S}} \hat{\mathbf{e}}_i \hat{\mathbf{e}}_i^\top \Sigma_{\tilde{\alpha}} \hat{\mathbf{e}}_j \hat{\mathbf{e}}_j^\top \tilde{\mathbf{S}}^\dagger \\ & + \tilde{\mathbf{S}} (\mathbf{I} - \hat{\mathbf{e}}_i \hat{\mathbf{e}}_i^\top) \Sigma_{\tilde{\gamma}} (\mathbf{I} - \hat{\mathbf{e}}_j \hat{\mathbf{e}}_j^\top) \tilde{\mathbf{S}}^\dagger. \end{aligned} \quad (27)$$

Note that all covariance matrices on the right hand side of (27), except  $\Sigma_{\tilde{d}}$ , are diagonal. In addition, the fact  $\Sigma_{\tilde{b}_{ij}} = \Sigma_{\tilde{b}_{ji}}^\dagger$  results in the expected Hermitian matrix  $\Sigma_{\text{vec}(\delta\mathbf{S})}$ .

We are now ready to propagate the error in the raw S-parameter  $\tilde{\mathbf{S}}$  to the error in the corrected S-parameter  $\tilde{\mathbf{S}}^c$ .  $\delta\mathbf{S}^c$  is approximately a linear transformation of  $\delta\mathbf{S}$ . Consequently,  $\text{vec}(\delta\mathbf{S}^c)$  remains to be a circularly-symmetric Gaussian random vector [14]. Uncertainty propagation is governed by

$$\Sigma_{\text{vec}(\delta\mathbf{S}^c)} = (\mathbf{R}^\top \otimes \mathbf{Q}) \Sigma_{\text{vec}(\delta\mathbf{S})} (\mathbf{R}^\top \otimes \mathbf{Q})^\dagger. \quad (28)$$

Matrices  $\mathbf{Q}$  and  $\mathbf{R}$  are explained in Appendix B. In essence, the matrix  $(\mathbf{R}^\top \otimes \mathbf{Q})$  corresponds to the Jacobian matrix that characterizes how sensitively  $\mathbf{S}^c$  responds to a small perturbation in  $\mathbf{S}$ .

## V. EXPERIMENTAL VERIFICATION

Obviously the theoretical developments merely remain an academic exercise without validation by experiments. In this section, experimental data measured by a two-port VNA are presented to check the veracity of the developed model. All the measurements were conducted with precision N-type connectors in the frequency range from 3 GHz to 6 GHz. An open-short-load-thru (OSLT) calibration was performed in order to resolve the VNA switch-error terms and error-box terms. The measurements of the OSLT standards were conducted at the highest possible SNR levels. As a result, the noise influence was minimized in the calibration stage. All the experiments were conducted in a laboratory with tightly

controlled environment. The lab temperature was set in the range of  $23 \text{ }^\circ\text{C} \pm 0.5 \text{ }^\circ\text{C}$  and the lab relative humidity was set in the range of  $40 \% \pm 5 \%$ . As such, the ambient condition was maintained and the instrument drift was minimized.

### A. Noise Waves in VNA

Prior to measurements of the DUTs, a large number of wave quantities were collected while both test ports of the VNA were terminated by matched loads. The matched loads acted like ambient noise sources with a known noise power level, approximately  $k_B T_0 \Delta f$  in the Rayleigh-Jeans limit. Here,  $k_B$  is the Boltzmann constant,  $T_0$  is the ambient temperature at 297 K, and  $\Delta f$  is the VNA IF bandwidth equal to 10 kHz. This ambient noise power level is about -134 dBm. Additionally, the power spectral density of all the electronic noise within 10 kHz was expected to be devoid of strong variation. A symmetry of the power spectral density about the frequency of interest can be assumed, so that the independence condition can be met between the real and the imaginary parts of the noise wave.

All eight wave quantities,  $\alpha_l(m)$  and  $\beta_l(m)$  ( $l, m = 1, 2$ ), were recorded, although only six of them were relevant to the study. The relevant noise waves are listed in Table I. The index on the subscript indicates the location of the receiver and the index in the parenthesis indicates which port is the stimulus port.

The stimulus power level was set in steps of 10 dBm from -10 dBm to -90 dBm on the VNA. At each power level, ten thousand redundant measurements were iterated. Next, data were processed to compute the statistical quantities listed in the first column of Table I. Note that six noise waves directly obtained from VNA were processed. They were  $\alpha_1(1)$ ,  $\alpha_2(1)$ ,  $\alpha_2(2)$ ,  $\beta_1(2)$  and  $\beta_2(1)$ . The magnitude of the sampled wave data were either squared and then averaged or averaged and then squared. The corresponding noise source components are listed in the second column of Table I. In this way, all the pertinent noise power levels can be extracted. These in turn can be used to calculate  $\sigma_a^2$  and  $\sigma_b^2$  in (11a) and (11b).

Experiment results at all frequencies were very similar. An example of processed data at 4 GHz is shown in Fig. 5. The following findings are of particular interest for determining the model parameters.

- 1) The SNR in  $\alpha_1(1)$  and  $\alpha_2(2)$  remained pretty much unchanged from -20 dBm to -80 dBm as shown in Fig. 5(A). This was primarily due to the specific VNA power leveling mechanism. The VNA source power could be tuned between -5 dBm to -10 dBm. For any desired stimulus power levels below that range, a series of 5 dB source attenuation were automatically inserted by the VNA. For example, the source power level at -7 dBm in combination with 25 dB attenuation resulted in a VNA excitation power of -32 dBm at the test port. The addition of attenuation was equivalent to adding the ambient noise while reducing both the existing signal and noise intrinsic to the VNA stimulus. As long as the impurity noise in the stimulus is much stronger than the ambient noise, the addition of attenuation would not degrade the SNR in the VNA stimulus. This was consistent with the observation.

TABLE II  
 VNA SIGNAL AND NOISE POWER LEVELS IN UNIT OF DBM

Port 1				Port 2			
$P_1^2$	$\langle  \tilde{s}_{n1} ^2 \rangle (\sim \sigma_{a1}^2)$	$\langle  \tilde{\alpha}_{n1} ^2 \rangle$	$\langle  \tilde{\beta}_{n1} ^2 \rangle$	$P_2^2$	$\langle  \tilde{s}_{n2} ^2 \rangle (\sim \sigma_{a2}^2)$	$\langle  \tilde{\alpha}_{n2} ^2 \rangle$	$\langle  \tilde{\beta}_{n2} ^2 \rangle$
-10	-81.2	-88.2	-90.7	-10	-79.9	-88.1	-90.2
-20	-85	-88.2	-90.6	-19.9	-82.9	-88.2	-90.2
-30	-81.2	-98.2	-90.6	-29.9	-93.1	-98.2	-90.2
-40	-105.5	-108	-90.7	-39.9	-102.9	-108	-90.3
-50	-115.7	-118	-90.7	-49.9	-113.4	-118	-90.2
-60	-125.7	-128	-90.6	-59.9	-121.7	-128	-90.3
-70	-135.2	-138	-90.7	-69.9	-133	-138	-90.2
-80	-144.9	-148	-90.6	-79.9	-142.2	-148	-90.2
-90	-135.3	-148	-90.6	-89.1	-133.2	-148	-90.2

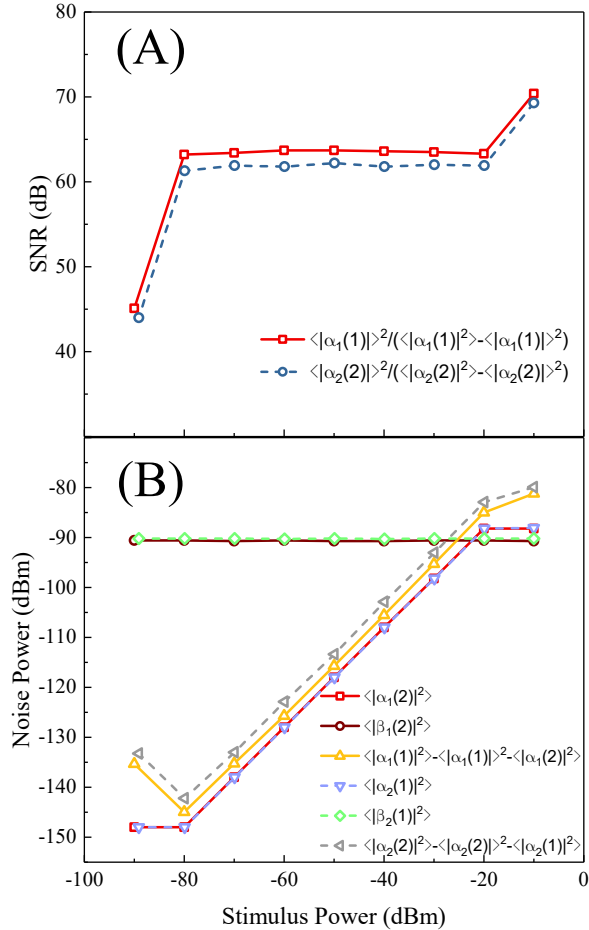


Fig. 5. Processed VNA data measured at 4 GHz. (A) Stimulus SNR for port 1 and 2. (B) Power levels of various noise signals. The SNR in the excitation signals remained mostly invariant of the excitation power levels.

- 2) Both variances,  $\langle |\alpha_1(2)|^2 \rangle$  and  $\langle |\alpha_2(1)|^2 \rangle$  (red and purple lines in Fig. 5(B)), decreased as the stimulus power was reduced. For stimulus power levels lower than -70 dBm, both of the noise power levels were lower than -134 dBm.<sup>2</sup> We therefore considered that the measured

<sup>2</sup>This was somewhat surprising in the sense that the combined VNA receiver and termination noise was lower than the ambient noise. Although this didn't deter us from complete our experimental investigation, we planned to reach out to the instrument maker for explanation and insight about this surprising observation.

$\langle |\alpha_1(2)|^2 \rangle$  and  $\langle |\alpha_2(1)|^2 \rangle$  were solely due to the receiver noise  $\langle |\tilde{\alpha}_{n1}|^2 \rangle$  and  $\langle |\tilde{\alpha}_{n2}|^2 \rangle$ , respectively.

- 3) The noise due to the stimulus impurity for Port 1 can be extracted by calculating  $\langle |\alpha_1(1)|^2 \rangle - \langle |\alpha_1(1)|^2 \rangle^2 - \langle |\alpha_1(2)|^2 \rangle$ . As shown in Fig. 5(B), the stimulus impurity noise (the yellow line) was consistently higher than the receiver noise (the red line) in Port 1. The same conclusion could be drawn for Port 2. We want to point out that the correlation condition  $\langle \tilde{a}_{nm}^* \tilde{b}_{nm} \rangle / (\langle |\tilde{a}_{nm}|^2 \rangle \langle |\tilde{b}_{nm}|^2 \rangle) \ll 1$  must hold for the independence between  $\tilde{a}_{nm}$  and  $\tilde{b}_{nm}$  to be valid. This condition was mostly met except two occasions at the two highest stimulus power settings. However, as shown in Section V-D, the noise influence was insignificant for measurements of S-parameters of a relatively large magnitude at these power levels.
- 4) Both variances  $\langle |\beta_1(2)|^2 \rangle$  and  $\langle |\beta_2(1)|^2 \rangle$  were mostly invariant when varying the stimulus power levels. In addition, they were much greater than -134 dBm. Therefore,  $\langle |\tilde{\beta}_{n1}|^2 \rangle \approx \langle |\beta_1(2)|^2 \rangle$  and  $\langle |\tilde{\beta}_{n2}|^2 \rangle \approx \langle |\beta_2(1)|^2 \rangle$ .

A summary of signal and noise power levels at different stimulus settings is listed in Table II. These values can be used as the model parameters to predict the behavior of noisy S-parameters. The comparison with the experimental data will be discussed in Section V-C.

### B. Independence Check

The model we developed also relies on the independence of the different noise waves. We used the multivariate version of Hoeffding's Phi-Square test on the measured VNA data [15]. In essence, the Phi-Square is an independence measure among a number of RVs. We denote the total number of RVs by  $D$ . For ease of notation, the RVs are populated in a  $D$ -dimensional random vector  $\mathbf{v}$  that is in the space of  $\mathbb{R}^D$ . The Phi-Square of  $\mathbf{v}$  is defined by

$$\Phi^2 = h(D) \int_{\mathbb{R}^D} [C(\mathbf{v}) - \Pi(\mathbf{v})]^2 d\mathbf{v}. \quad (29)$$

Here,  $C(\mathbf{v})$  is the joint CDF and  $\Pi(\mathbf{v})$  is the product of the individual CDFs of  $\mathbf{v}$ .  $h(D)$  is a function of the dimension number  $D$  and its value constrains  $\Phi^2$  in the interval of  $[0, 1]$ .

For mutually independent RVs, the joint distribution of  $D$  RVs is a product of  $D$  multivariate marginals. In other words,

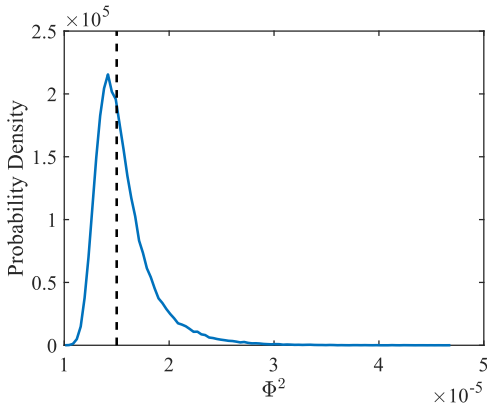


Fig. 6. Phi-Square tests on 8 random variables independently generated by a computer. The histogram of the Phi-Square values was obtained from 100000 realizations.  $\Phi^2 = 1.5 \times 10^{-5}$  is marked with a dashed line. The comparison indicates that various noise waves are independent.

the mutual independence among  $\mathbf{v}$  is equivalent to  $C(\mathbf{v}) = \Pi(\mathbf{v})$  and therefore the Phi-Square would be zero.

For practical applications, the Phi-Square test needs to be numerically implemented in order to estimate  $C(\mathbf{v})$  and  $\Pi(\mathbf{v})$  from RV data. For example, we deal with a total of  $N$  samples of  $D$ -dimensional random vectors:  $\mathbf{v}_1, \dots, \mathbf{v}_N$ , so that the empirical Phi-Square  $\hat{\Phi}^2$  can be estimated by [15], [16]

$$\hat{\Phi}^2 = h(D) \left\{ \frac{1}{N^2} \sum_{j=1}^N \sum_{k=1}^N \prod_{i=1}^D [1 - \max(V_{ij}, V_{ik})] - \frac{2}{N} \frac{1}{2^D} \sum_{j=1}^N \prod_{i=1}^D (1 - V_{ij}^2) + \frac{1}{3^D} \right\}. \quad (30)$$

$V_{ij}$  is the probability inferred from the ranks of  $v_{ij}$  in all observations of the  $i$ -th RV, which is calculated by  $(\text{rank of } v_{ij} \text{ in } v_{i1}, \dots, v_{iN})/N$ .

We separated the four receiver waves into their real and imaginary parts and recast them into a vector. The four waves were  $\alpha_1(2)$ ,  $\beta_1(2)$ ,  $\alpha_2(1)$  and  $\beta_2(1)$ . As such, we had ten thousand samples of  $8 \times 1$  random vectors  $\mathbf{v}$  at each VNA power level.

The empirical estimator of the Phi-Square from samples of a finite size ( $N = 10000$  in this case) wouldn't be exactly zero for mutually independent RVs. For all the noise data, the Phi-Square values were mostly less than  $1.5 \times 10^{-5}$ . The largest Phi-Square value was  $2.3 \times 10^{-5}$  when the power level was set to -30 dBm and the frequency was at 3 GHz.

The obtained Phi-Square values were meaningless without comparing to that of known independent RVs. We applied the Phi-Square test on computer generated  $8 \times 1$  independent random vectors with the same sample size of ten thousand. We simulated 100000 realizations and plotted the histogram of Phi-Square values in Fig. 6. The median of simulated Phi-Squares was about  $1.5 \times 10^{-5}$ . This fact implied that most experimental RVs showed an independence better than the half of the RV independently generated by the computer. As a result, we were very confident that the noise waves measured on the VNA were indeed mutually independent.

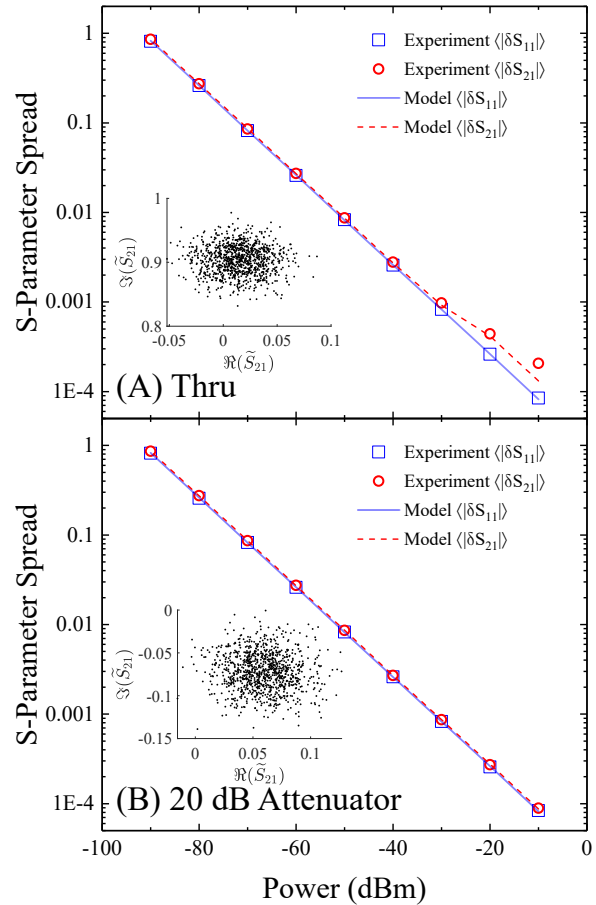


Fig. 7. Comparison between experiments and models of the spread of raw S-parameters due to noise at 4 GHz. (A) Thru. (B) 20 dB Attenuator. The insets illustrate examples of scattered  $S_{21}$  measurements due to the noise.

### C. Noisy S-Parameter At Various SNR

After we validated multiple assumptions made in the VNA noise model, we proceeded to check how well the model would predict the noise influence in the S-parameter measurements. As mentioned in Section III-B, the mean spread of the scattered S-parameter can be a good indicator for evaluation. We measured two devices; a thru and a 20 dB attenuator. The VNA power setting was varied from -10 dBm to -90 dBm by 10 dBm per step. At each step, we measured two-port S-parameters ten thousand times. Next, the data were processed to obtain the mean of the noisy S-parameter spread,  $\langle |\delta S| \rangle$ .

For modeling, we can substitute the pertinent signal and noise power levels listed in Table II into (9) and (18) to calculate the model prediction. Alternatively, we can also take the square root of the diagonal elements of the covariance matrix in (26) and scale the results by a factor of  $\sqrt{\pi}/2$  (see the discussion following (18)). We ended up using the latter approach, since the covariance matrix could be further used for the uncertainty propagation in the following Section V-D.

An illustrative example of the comparison between the model and the experiments is shown in Fig. 7. Overall, we reached an excellent agreement for both devices at most of the stimulus power levels. A few noteworthy points are addressed here.

- 1) Except for a couple of points in the thru data at the high stimulus power levels, the mean of the radius of noisy S-parameters grew logarithmically as the stimulus power decreased. This is as expected by the model prediction in (18). For these points, the variance  $\sigma_b^2$  was primarily due to the detector noise of the test-port receivers, (i.e.  $\sigma_b^2 \sim \langle |\tilde{\beta}_n|^2 \rangle$ ). All other noise components are negligibly weak. Thus, the SNR with the respect to the noise power in  $\tilde{b}_n$  is roughly  $\langle |\tilde{\beta}_n|^2 \rangle / P^2$ . As shown in Table II, the noise strength measured by the test-port receiver was mostly constant independent of the stimulus power. Therefore, the SNR reduced linearly as the stimulus power decreased, which in-turn led to a linear growth of the radius  $\langle |\delta S| \rangle$ .
- 2) The experimental data showed that the values of  $\langle |\delta S_{21}| \rangle$  were always slightly larger than those of  $\langle |\delta S_{11}| \rangle$ . The same relation was applicable to  $\langle |\delta S_{12}| \rangle$  and  $\langle |\delta S_{22}| \rangle$ . The reason can be inferred from the model by checking the elements in the covariance matrix  $\Sigma_{\text{vec}(\delta S)}$ . The difference of the first two diagonal elements is

$$\langle |\delta S_{21}|^2 \rangle - \langle |\delta S_{11}|^2 \rangle \approx (|\bar{S}_{21}|^2 - |\bar{S}_{11}|^2) \frac{\langle |\tilde{\alpha}_{n1}|^2 \rangle}{P_1^2}. \quad (31)$$

For the thru and the attenuator used in the experiments,  $|\bar{S}_{21}| > |\bar{S}_{11}|$  held at all measured frequencies. Consequently, the noisy S-parameter  $\tilde{S}_{21}$  (or  $\tilde{S}_{12}$ ) had a slightly larger spread than  $\tilde{S}_{11}$  (or  $\tilde{S}_{22}$ ).

- 3) In the experiments, the values of  $\langle |\delta S_{21}| \rangle$  for the thru ticked up away from the linear line at the stimulus power of -30 dBm, -20 dBm and -10 dBm. However, this phenomenon didn't appear for the attenuator. Again, the model clearly predicted what exactly happened. Referring to the second diagonal element of  $\Sigma_{\text{vec}(\delta S)}$ , it contains a term  $|\bar{S}_{21}|^2 \langle |\tilde{\alpha}_{n1}|^2 \rangle / P_1^2$ . This term became appreciable only for the thru when  $\langle |\tilde{\alpha}_{n1}|^2 \rangle$  was comparable to or larger than  $\langle |\tilde{\beta}_{n1}|^2 \rangle$ . For the attenuator, the transmission magnitude  $|\bar{S}_{21}|^2$  was small. Even if the noise power  $\langle |\tilde{\alpha}_{n1}|^2 \rangle$  was larger than  $\langle |\tilde{\beta}_{n1}|^2 \rangle$ , its attenuated contribution was insignificant. We were able to very closely predict the experimental results when the stimulus power was at -30 dBm and -20 dBm as shown in Fig. 7(A). The prediction was slightly off at the -10 dBm power level. We suspected that  $\langle |\tilde{\alpha}_{n1}|^2 \rangle$  might be underestimated from experiments at -10 dBm power level. Nevertheless, the prediction by the model was much less critical for the thru at this power level. This claim will be evident from the uncertainty perspective discussed in the next section.

#### D. Uncertainty Analysis

We have so far validated the noisy S-parameter model developed in Section II. In this subsection, we want to reiterate the importance of the uncertainty due to the noise by comparing it to the conventional uncertainty estimates without including noise. We used the Microwave Uncertainty Framework (MUF) to obtain the conventional uncertainty due to the non-idealities of the calibration standards [17]. The

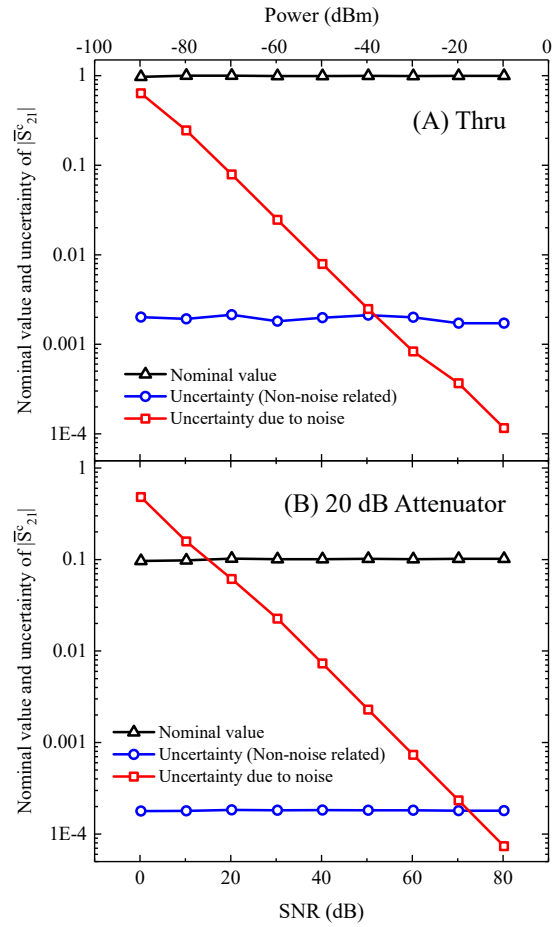


Fig. 8. (A) Calibrated S-parameter of the thru at 4 GHz. (B) Calibrated S-parameter of the 20 dB attenuator at 4 GHz. Note that the SNR corresponds to  $P_1^2 / \sigma_{b2}^2$  or roughly  $P_1^2 / \langle |\tilde{\beta}_{n2}|^2 \rangle$ . The uncertainty associated with noise is critical for attenuation measurements even at a relatively high SNR.

uncertainty due to the noise was propagated according to the formula developed in (28). An example of the magnitude of the transmission parameter  $|\bar{S}_{21}|$  of the devices is shown in Fig. 8. The calculation of this specific uncertainty is explained in Appendix C.

Referring to (41) in Appendix B, we can roughly express the error in the corrected S-parameter as follows.

$$\delta S^c \approx \sqrt{|\bar{S}|^2 (\delta T)^2 + |T|^2 (\delta S)^2}, \quad (32)$$

where  $\delta T$  is associated with the conventional uncertainty mainly due to the imperfections in calibration standards and  $\delta S$  is the uncertainty due to the noise. Note that we didn't really use (32) to calculate the overall uncertainty. Rather, this equation helped us gain insight of how the different uncertainty components play a role in the overall uncertainty when different kinds of devices were measured. These two uncertainty contributions corresponded to the blue line and the red line, respectively, in Fig. 8.

As shown in Fig. 8, while the conventional uncertainty roughly remained at a constant level, the uncertainty due to the noise increased as the stimulus power was reduced, or equivalently as the VNA SNR was reduced. This is again not surprising. The conventional uncertainty should be invariant

of VNA SNR levels once the calibration was completed. However, the uncertainty due to the noise is highly dependent on the SNR of the VNA as shown in Section III. We can roughly estimate the uncertainty at a specific SNR by taking the inverse of the square root of the SNR value. For example, the uncertainty at 60 dB SNR is roughly 0.001, which corresponded to the stimulus power level at -30 dBm in Fig. 8. At this power level, the uncertainty due to the noise was fairly appreciable for including it in the uncertainty analysis for the thru. As shown in Fig. 8(A), the uncertainty due to the noise became dominant when the SNR was further reduced. At the extreme of the lowest SNR, the uncertainty due to the noise was even comparable to the nominal value of  $|S_{21}^c|$ .

As shown in Fig. 8(B), the dominance of the uncertainty due to the noise arrived at a much higher SNR level for the VNA measurements on the attenuator. On one hand, the contribution of the conventional uncertainty was commensurate with the magnitude of the S-parameter as shown in (32). Because of a much lower  $|S_{21}|$  for the attenuator, the conventional uncertainty for the attenuator was about one order of magnitude smaller than the conventional uncertainty for the thru. On the other hand, the contribution of the uncertainty due to the noise, scaled by the same transmission coefficient in (32), remained pretty much the same for both the thru and the attenuator. As a result, the uncertainty due to the noise was non-negligible for the attenuator even at 80 dB SNR and became the primary component at the SNR levels of 70 dB and less. As a matter of fact, the conventional uncertainty can even be safely neglected at the stimulus power levels of -30 dBm or lower, corresponding to the SNR of no more than 60 dB. This fact substantiates the assertion made in Section I. The uncertainty due to the noise is sometimes critical in VNA measurements. This is particularly true for S-parameters of a small magnitude, such as the reflection off an absorber and the transmission through an attenuator.

## VI. DISCUSSION AND REMARKS

All the experiments presented here were conducted on passive DUTs. If we were to measure S-parameters of an active device, such as an amplifier, we would have to know its noise waves or at least its noise figure. It is expected that measurements of amplification and the output-port reflection of the amplifier are subject to stronger noisy conditions than what is normally encountered in dealing with passive devices.

The high SNR condition is often associated with the use of high stimulus power levels. Such a condition may not be met in some specific, but not uncommon, circumstances. For example, the measurements of wave parameters and S-parameters above 67 GHz require a VNA instrument equipped with extension modules. The stimulus power level is very limited at high frequencies. Therefore, the SNR associated with VNAs at high frequencies is usually not as high as those at low frequencies. Even for VNA measurements at low frequencies, the use of low stimulus power is sometimes preferred to avoid harmonics and saturation of active devices. Under all these circumstances, it is important to estimate the noise-contributed uncertainty by use of the SNR of the

VNA. This estimation can help us decide whether or not the uncertainty due to the noise warrants consideration.

The propagation of uncertainty was formulated by transforming the covariance matrix, equivalent to the sensitivity analysis in the MUF. This approach is only valid for linear operations on variables and operations of insignificant nonlinearity. The circular symmetry specific to noise-related random variables is no longer maintained under nonlinear operation. As a consequence, the real covariance matrix of the real and the imaginary parts of the complex variables, instead of the complex covariance matrix, needs to be used [18], [19]. Furthermore, once the nonlinearity becomes significant, it is critical to conduct numerical samplings to simulate the random processes by use of the Monte Carlo method. Next, a statistical analysis can be performed on the simulated data to extract propagated uncertainty values.

Measurements of all wave parameters are recommended for versatility and convenience even if S-parameters are ultimately needed<sup>3</sup>. The switch-term correction is not required for the calibration involving wave parameters. This is advantageous because the switch-term correction becomes exponentially complicated as the port number increases. Consequently, it makes a lot of sense to assign noise-induced RV terms to the wave quantities and track them numerically in the practical implementation. This also allows us to eliminate several modeling approximations we have made in this investigation. Furthermore, the noise-induced uncertainty can be included in the calibration stage as well. Although it is minimal for measurements on most calibration standards, the noise effect may be significant for S-parameter measurements on specific components such as calibration loads.

## VII. CONCLUSION

For the first time, we have established a comprehensive model to include noise effects in S-parameter measurements by a VNA. The model includes a variety of noise sources and the overall noise contribution to the S-parameter emerges as a ratio between a zero-mean RV and a non-zero-mean RV. Both RVs are the complex Gaussian type. The statistical analysis shows that such a complex Gaussian ratio approaches the complex normal distribution at moderate and high SNR levels. However it deviates from the complex normal distribution at low SNR levels.

A number of statistical quantities of the complex Gaussian ratio have been derived for model validation and uncertainty estimation. For ordinary measurement conditions, the uncertainties of the real and imaginary parts of the S-parameter are identical and uncorrelated. The uncertainty value can be estimated by the root square of the NSR. For passive devices, this NSR is approximately the ratio between the detection noise power of the test-port receiver and the signal power of the VNA stimulus.

We designed and implemented a series of experiments on a two-port VNA to validate model assumptions and extract

<sup>3</sup>However, it is not practical to measure all wave parameters on an economical VNA with the reduced number of receivers. For example, a two-port VNA with three receivers.

model parameters. These parameters were fed to the model to predict the noisy S-parameter behaviors. We reached an excellent agreement of the mean of the noisy S-parameter spread between experiments and predictions. Furthermore, it was shown that the impact of noise is of vital importance in S-parameter measurements. This is in particular crucial for S-parameters of small magnitudes.

A full inclusion of noise effects in the VNA measurements requires a reliable numerical tool. The NIST MUF software is a good candidate to implement noise contributions systematically for the data processing and uncertainty analysis. The procedure outlined in Section V-A can be followed to determine the variance values of various noise sources. These parameters can be attached to the raw waves measured by the VNA as the uncertainty due to the noise. Subsequently, all the derived quantities will contain the uncertainty component contributed by the noise. The uncertainty correlations, if any, are preserved as well.

#### APPENDIX A

##### S-PARAMETER INCLUDING NOISE COMPONENTS

In this appendix, we show how (8) is obtained. We start by writing out the  $m$ -th element of  $\alpha$  and  $m'$ -th element of  $\beta$  as follows.

$$\alpha_m = \left[ (\mathbf{I} - \Gamma \bar{\mathbf{S}})^{-1} \right]_{mm} P_m + \tilde{s}_{nm} + \tilde{\alpha}_{nm}, \quad (33a)$$

$$\begin{aligned} \beta_{m'} = & \sum_{l=1}^M \bar{S}_{m'l} \left[ (\mathbf{I} - \Gamma \bar{\mathbf{S}})^{-1} \right]_{lm} P_m + \tilde{d}_{nm'} + \tilde{\beta}_{nm'} \\ & + \bar{S}_{m'm} \tilde{s}_{nm} + \sum_{\substack{l=1 \\ l \neq m}}^M \bar{S}_{m'l} \tilde{t}_{nl}. \end{aligned} \quad (33b)$$

Anticipating the division by  $\alpha_m$ , we rewrite (33b) as

$$\begin{aligned} \beta_{m'} = & \bar{S}_{m'm} \left[ (\mathbf{I} - \Gamma \bar{\mathbf{S}})^{-1} \right]_{m'm} P_m + \bar{S}_{m'm} \tilde{s}_{nm} \\ & + \bar{S}_{m'm} \tilde{\alpha}_{nm} - \bar{S}_{m'm} \tilde{\alpha}_{nm} \\ & + \sum_{\substack{l=1 \\ l \neq m}}^M \bar{S}_{m'l} \left[ (\mathbf{I} - \Gamma \bar{\mathbf{S}})^{-1} \right]_{lm} P_m + \tilde{d}_{nm'} \\ & + \tilde{\beta}_{nm'} + \sum_{\substack{l=1 \\ l \neq m}}^M \bar{S}_{m'l} \tilde{t}_{nl} \\ = & \bar{S}_{m'm} \left\{ \left[ (\mathbf{I} - \Gamma \bar{\mathbf{S}})^{-1} \right]_{m'm} P_m + \tilde{s}_{nm} + \tilde{\alpha}_{nm} \right\} \\ & + \sum_{\substack{l=1 \\ l \neq m}}^M \bar{S}_{m'l} \left[ (\mathbf{I} - \Gamma \bar{\mathbf{S}})^{-1} \right]_{lm} P_m \\ & + \tilde{d}_{nm'} + \tilde{\beta}_{nm'} - \bar{S}_{m'm} \tilde{\alpha}_{nm} + \sum_{\substack{l=1 \\ l \neq m}}^M \bar{S}_{m'l} \tilde{t}_{nl}. \end{aligned} \quad (34)$$

As such, the three terms in (8) follow evidently.

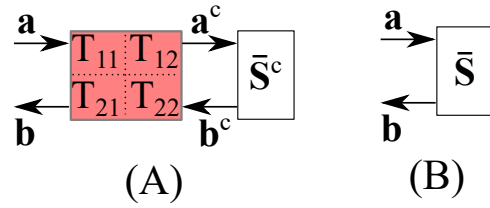


Fig. 9. (A) A  $M$ -port DUT of the S-parameter  $\bar{\mathbf{S}}^c$  is embedded in the VNA error box ( $2M$ -port network) marked in red. (B) An equivalent network shows VNA raw waves and the uncorrected S-parameter  $\bar{\mathbf{S}}$ .

#### APPENDIX B

##### MULTI-PORT DE-EMBEDDING

The error correction routine in VNA measurements can be generalized as a multiport de-embedding process. The waves associated with the  $M$ -port DUT are embedded in a  $2M$ -port network as shown in Fig. 9. The  $2M$ -port network represents the physical VNA error boxes. The VNA raw waves are the measurands immediately accessible in the measurements. Error corrections are equivalent to de-embedding the corrected S-parameters (or corrected wave parameters) from raw S-parameters (or raw wave parameters).

We use the transfer matrix to facilitate handling the cascaded multi-ports. The raw VNA waves  $\mathbf{a}$  and  $\mathbf{b}$  are the waves on the left side of the  $2M$ -port network, while the corrected waves  $\mathbf{a}^c$  and  $\mathbf{b}^c$  are on the right side. They are related by the transfer matrix via

$$\begin{bmatrix} \mathbf{b} \\ \mathbf{a} \end{bmatrix} = \begin{bmatrix} \mathbf{T}_{11} & \mathbf{T}_{12} \\ \mathbf{T}_{21} & \mathbf{T}_{22} \end{bmatrix} \begin{bmatrix} \mathbf{b}^c \\ \mathbf{a}^c \end{bmatrix} \quad (35)$$

In addition, these wave parameters are used to define the raw and corrected S-parameters.

$$\mathbf{b} = \bar{\mathbf{S}} \mathbf{a}, \quad (36a)$$

$$\mathbf{b}^c = \bar{\mathbf{S}}^c \mathbf{a}^c, \quad (36b)$$

Elimination of waves in (35), (36a) and (36b) leads to

$$\bar{\mathbf{S}}^c = (\mathbf{T}_{11} - \bar{\mathbf{S}} \mathbf{T}_{21})^{-1} (\bar{\mathbf{S}} \mathbf{T}_{22} - \mathbf{T}_{12}). \quad (37)$$

All the sub-matrices of the transfer matrix can be determined from the VNA calibration. Overall, the uncertainties in  $\bar{\mathbf{S}}^c$  are due to the uncertainty in all  $\mathbf{T}$ 's and the uncertainty in  $\bar{\mathbf{S}}$ . The uncertainty in  $\mathbf{T}$ 's mostly come from the dimensional uncertainty of the calibration standards. The uncertainty in  $\bar{\mathbf{S}}$  is what this paper concerns. Therefore, we only need to focus on how the uncertainty in  $\bar{\mathbf{S}}$  affects the uncertainty in  $\bar{\mathbf{S}}^c$ .

As shown in (37),  $\bar{\mathbf{S}}^c$  is a nonlinear function of  $\bar{\mathbf{S}}$ . Although the relation can be approximately linearized, we preserve all nonlinear terms in differentiation for rigor. Applying the partial matrix derivative on  $\bar{\mathbf{S}}^c$  in (37) with respect to  $\bar{\mathbf{S}}$ , we get

$$\delta \bar{\mathbf{S}}^c = \mathbf{Q} (\delta \bar{\mathbf{S}}) \mathbf{R}. \quad (38)$$

Here, matrices  $\mathbf{Q}$  and  $\mathbf{R}$  are given by [20]

$$\mathbf{Q} = (\mathbf{T}_{11} - \bar{\mathbf{S}} \mathbf{T}_{21})^{-1}, \quad (39a)$$

$$\mathbf{R} = \mathbf{T}_{21} \bar{\mathbf{S}}^c + \mathbf{T}_{22}, \quad (39b)$$

After vectorization for calculating the covariance matrix, we reach

$$\text{vec}(\delta\mathbf{S}^c) = (\mathbf{R}^T \otimes \mathbf{Q})\text{vec}(\delta\mathbf{S}). \quad (40)$$

From the above equation, the uncertainty propagation expressed in (28) follows immediately.

Since the typical VNA error boxes are close to transmission lines with good port matches, the  $\mathbf{T}$  matrix in (35) is roughly block diagonal and the following linear relation approximately holds.

$$\bar{\mathbf{S}}^c \approx \mathbf{T}_{11}^{-1} \bar{\mathbf{S}} \mathbf{T}_{22}. \quad (41)$$

As a consequence, the sensitivity analysis by the covariance-matrix transformation is adequate for the uncertainty estimation.

#### APPENDIX C UNCERTAINTY OF S-PARAMETER MAGNITUDE

Taking the magnitude of a complex variable is a nonlinear operation. As a consequence, the higher-order terms in the Taylor series may impact the propagation of the uncertainty. Although it's a common practice to numerically propagate the uncertainty in the S-parameters to the uncertainty in the magnitude of the S-parameters, we can actually calculate the variance of the magnitude of the S-parameters analytically from the statistical properties of the residual error. By definition, the variance of  $|\tilde{S}^c|$  is

$$\left\langle \left( |\tilde{S}^c| - \langle |\tilde{S}^c| \rangle \right)^2 \right\rangle = \left\langle |\tilde{S}^c|^2 \right\rangle - \left\langle |\tilde{S}^c| \right\rangle^2. \quad (42)$$

Here, the noisy S-parameter  $\tilde{S}^c$  has two components; the nominal value  $\bar{S}^c$  and the complex Gaussian RV  $\delta S^c$ .

Without changing its magnitude, we apply a phase shift on the noisy S-parameter as follows

$$\tilde{S}^c e^{-j \cdot \text{Arg}(\bar{S}^c)} = \left| \bar{S}^c \right| + \delta S^c e^{-j \cdot \text{Arg}(\bar{S}^c)}. \quad (43)$$

As such, the problem is analogous to studying the modulus of the sum of a non-negative number and a rotated complex Gaussian RV. It is well-known that the statistical properties of a complex Gaussian RV are invariant to phase rotations. Therefore, the magnitude of the noisy S-parameter is equivalently a Rice RV. Its variance is given by [21]

$$\begin{aligned} \left\langle |\tilde{S}^c|^2 \right\rangle - \left\langle |\tilde{S}^c| \right\rangle^2 = \\ \left| \bar{S}^c \right|^2 + \left\langle |\delta S^c|^2 \right\rangle - \frac{\pi \left\langle |\delta S^c|^2 \right\rangle}{4} L_{\frac{1}{2}}^2 \left( -\frac{\left| \bar{S}^c \right|^2}{\left\langle |\delta S^c|^2 \right\rangle} \right). \end{aligned} \quad (44)$$

Here,  $L_{\frac{1}{2}}(\cdot)$  is the Laguerre polynomial of the degree of 1/2. The values of  $\left\langle |\delta S^c|^2 \right\rangle$  are directly obtainable from the covariance matrix  $\Sigma_{\text{vec}(\delta\mathbf{S}^c)}$  in (28). By taking the square root of (44), we get the uncertainty of the corrected S-parameter magnitude due to the noise.

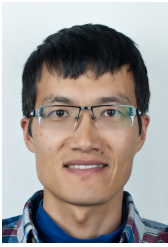
#### ACKNOWLEDGEMENT

We acknowledge Jeffrey Boulton at the Air Force Metrology and Calibration Program Office for inspiring the authors to look into this investigation. We also thank D. Williams and P. Hale at the RF Technology Division of NIST Boulder for valuable discussions on the network analysis and the uncertainty analysis.

The work of this publication is supported by NIST, an agency of the U.S. government, and is not subject to the U.S. copyright.

#### REFERENCES

- [1] D. K. Rytting, "Improved RF Hardware and Calibration Methods for Network Analyzers," *RF and Microwave Measurement Symposium and Exhibition*, Hewlett and Packard, 1991.
- [2] M. Garelli and A. Ferrero, "A Unified Theory for S-Parameter Uncertainty Evaluation," *IEEE Trans. Microw. Theory Techn.*, vol. 60, no. 12, pp. 3844-3855, Dec. 2012.
- [3] O. Marinov, "Noise partition in S-parameter measurement," *2013 22nd International Conference on Noise and Fluctuations (ICNF)*, Montpellier, 2013, pp. 1-4.
- [4] D. Nopchinda, T. Eriksson, H. Zirath and K. Buisman, "Measurement of Reflection and Transmission Coefficients Using Finite Impulse Response Least-Squares Estimation," *IEEE Trans. Microw. Theory Techn.*, vol. 68, no. 1, pp. 222-235, Jan. 2020.
- [5] J. Randa, "Noise characterization of multiport amplifiers," *IEEE Trans. Microw. Theory Techn.*, vol. 49, no. 10, pp. 1757-1763, Oct 2001.
- [6] H. Bosma, "On the theory of linear noisy systems," in *Philips research reports: Supplements*, Issue 10, 1967.
- [7] R. E. Ziemer and W. H. Tranter, *Principles of Communications: Systems, Modulation, and Noise*, 7th Ed., Hoboken, NJ: John Wiley & Sons, 2015, ch. 7, pp. 308-348.
- [8] J. A. Jargon, D. F. Williams and A. Sanders, "The Relationship Between Switch-Term-Corrected Scattering-Parameters and Wave-Parameters Measured With a Two-Port Vector Network Analyzer," *IEEE Microw. Wireless Compon. Lett.*, vol. 28, no. 10, pp. 951-953, Oct. 2018.
- [9] S. O. Rice, "Mathematical analysis of random noise," in *The Bell System Technical Journal*, vol. 24, no. 1, pp. 46-156, Jan. 1945.
- [10] D. Gu, "On The Quotient of Centralized and Non-Centralized Complex Gaussian Random Variables," *Journal of Research of NIST*, to be published.
- [11] F. W. J. Olver and L.C. Maximon, "Bessel functions," in *NIST Handbook of Mathematical Functions*, F. J. Olver, D. W. Lozier, R. F. Boisvert, and C. W. Clark, Eds. Cambridge, UK: Cambridge University Press, 2010, ch. 10, pp. 215-287.
- [12] C. L. Holloway, D. A. Hill, J. M. Ladbury, P. F. Wilson, G. Koepke and J. Coder, "On the Use of Reverberation Chambers to Simulate a Rician Radio Environment for the Testing of Wireless Devices," *IEEE Trans. Antennas Propag.*, vol. 54, no. 11, pp. 3167-3177, Nov. 2006.
- [13] "Calculating VNA measurement accuracy," Anritsu Application Note No. 11410-00464, 2008.
- [14] R. G. Gallager, *Principles of Digital Communication*, 1st ed., Cambridge, UK: Cambridge University Press, 2008.
- [15] S. Gaißer, M. Ruppert, and F. Schmid, "A multivariate version of Hoeffdings Phi-Square," *Journal of Multivariate Analysis*, vol. 101, no. 10, pp. 2571-2586, Nov. 2010.
- [16] C. Genest, J.-F. Quessy, and B. Rémillard. "Asymptotic Local Efficiency of Cramér-Von Mises Tests for Multivariate Independence," *The Annals of Statistics*, vol. 35, no. 1 pp. 166-191, Feb. 2007.
- [17] D. F. Williams, "NIST Microwave Uncertainty Framework," <https://www.nist.gov/services-resources/software/wafer-calibration-software>, accessed Dec. 1st, 2019.
- [18] N. M. Ridler and M. J. Salter, "An approach to the treatment of uncertainty in complex S-parameter measurements," *Metrologia*, vol. 39, no. 3, pp. 295-302, June 2002.
- [19] D. F. Williams *et al.*, "Covariance-based uncertainty analysis of the NIST electrooptic sampling system," *IEEE Trans. Microw. Theory Techn.*, vol. 54, no. 1, pp. 481-491, Jan. 2006.
- [20] A. Hjørungnes, *Complex-Valued Matrix Derivatives*, 1st ed., Cambridge, UK: Cambridge University Press, 2011.
- [21] S. O. Rice, "Statistical properties of a sine wave plus random noise," in *The Bell System Technical Journal*, vol. 27, no. 1, pp. 109-157, Jan. 1948.



**Dazhen Gu** (Senior Member, IEEE) received the Ph.D. degree in electrical engineering from University of Massachusetts, Amherst, in 2007.

He has been with the RF Technology Division, National Institute of Standards and Technology, Boulder, CO, since November 2003. During the first three and a half years, he did his doctoral research in development of terahertz imaging components and systems. From 2007 to 2009, he was with the Microwave Measurement Services project, where he was involved in microwave metrology, in particular thermal noise measurements and instrumentation. From 2009 to 2015, he took a position in the microwave remote-sensing project, in which a microwave brightness-temperature standard was successfully demonstrated. From 2015 to 2018, he was in charge of the microwave power project and developed the NIST power traceability with correlated uncertainties for 5G communication researches. Since March 2018, he has been with the Shared-Spectrum Metrology Group, where he is involved in the Spectrum Sensing and Noise Project.



**Jeffrey A. Jargon** (Senior Member, IEEE) received the B.S., M.S., and Ph.D. degrees in electrical engineering from the University of Colorado at Boulder in 1990, 1996, and 2003, respectively.

He has been a Staff Member of the National Institute of Standards and Technology (NIST), Boulder, CO, since 1990 and has conducted research in the areas of vector network analysis, optical performance monitoring, and waveform metrology. He is presently a member of the High-Speed Measurements Project in the Communications Technology Laboratory. Jeffrey was the recipient of six best paper awards, an URSI Young Scientist Award, and a Department of Commerce Silver Medal Award. He is a Senior Member of IEEE, a registered Professional Engineer in the State of Colorado, and an ASQ Certified Quality Engineer.



**Matthew J. Ryan** was born near Chicago, IL in April of 1998. He received a B.S. degree with honors in aerospace engineering and minors in computer science and applied mathematics from the University of Colorado Boulder in May of 2020. As a student, Matthew worked in the Aerospace Mechanics Research Center until 2019, when he moved to NIST under the RF Technology division. He now plans to work in industry for a few years before seeking a graduate degree.



**Anouk Hubrechs** received a BSc and MSc degree in Electrical Engineering at the Eindhoven University of Technology in 2017 and 2019, respectively. She was a foreign guest researcher in 2019 at the National Institute of Standards and Technology (NIST), where she worked on reverberation-chamber metrology. She is currently working as a PhD researcher on the AMICABLE project, researching interference effects in cable bundles. In 2019, she received the regional and district Zonta Women in Technology awards. She is currently vice-chair of Women in

Engineering IEEE Benelux.